Supplemental Information for

Superhalide Structure and Iodide-Proof Interphase *via* Electrolyte Regulation Enable Ultrastable Zinc-Iodine Batteries

Wenjing Deng[a], *Renfei Feng*[b], *and Xiaolei Wang*[a,*]

a. Department of Chemical and Materials Engineering, University of Alberta, 9211-116 Street NW., Edmonton, Alberta T6G 1H9, Canada
E-mail: xiaolei.wang@ualberta.ca

b. Canadian Light Source Inc., 44 Innovation Blvd., Saskatoon, Saskatchewan S7N 0X4, Canada

1. Experiment Procedure

Materials: methanol (MeOH), tetrabutylammonium iodide (TI), zinc trifluoromethanesulfonate ($Zn(OTf)_2$), and iodine, tetramethylammonium iodide, active carbon, Zn foils, glass microfiber filter, carbon cloth, Cu foil.

1.1 Electrolyte preparation

MeOH-TI electrolyte was prepared using methanol as solvent, 0.1 M TI as iodide salt and 1 M $Zn(OTf)_2$ as zinc salt. For high iodide loading and small N/P ratio test, 0.35 M and 0.55 M TI were applied. The HOH electrolyte was prepared by adding 1 M $Zn(OTf)_2$ in water solvent. MeOH-ZnI_2 electrolyte was prepared using methanol as solvent, 0.05 M ZnI_2 as iodide salt to keep the same iodide amount and 1M $Zn(OTf)_2$ as zinc salt.

1.2 Preparation of cathode

For the cathode, carbon cloth was washed with ethanol and dried in oven. A slurry mixed by active carbon, Super P carbon, and polyvinyl difluoride at a weight ratio of 7:2:1 in NMP solvent was coated on carbon cloth to prepare the cathodes.

1.3 Characterization

Spectral characterizations of the electrolytes were acquired by FTIR spectroscopy on Nicolet iS50 infrared spectroscopy instrument. Raman spectroscopy (Horiba LabRAM HR Evolution) using 632.8 nm laser and ^1H Nuclear magnetic resonance spectrum (NMR) on a Bruker AVANCE III spectrometer using 400 MHz. X-ray Diffraction (XRD) measurement was conducted on an Ultima IV (Rigaku) diffractometer equipped with a Cu Kα X-ray source. X-ray spectrometer (XPS, Kratos AXIS Ultra) was used to gain insight into the chemical binding environment of elements. The micro/nano-structures of prepared materials were characterized by scanning electron microscope (SEM, Zeiss EVO M10), field-emission scanning electron microscope (FESEM, Zeiss Sigma). The surface wettability of anode materials was measured by contact angle measuring system (Dataphysics

OCA50). The X-ray absorption spectra (XAS) including X-ray absorption near-edge structure (XANES) and extended X-ray absorption fine structure (EXAFS) of the samples at Zn K-edge (9659 eV were collected at the Canada Light Source (CLS) center. The Zn K-edge XANES data were recorded in a transmission mode. Zn foil and ZnO were used as references. The acquired EXAFS data were extracted and processed according to the standard procedures using the ATHENA module implemented in the software packages.

1.4 Fabrication of batteries and electrochemical measurements

For the asymmetrical cell, the bare Cu was used as a working electrode with electrolyte and Zn foil as a counter electrode. For the symmetrical cell, the Zn foils was punched into disks and used as electrodes subsequently and the electrolyte was composited of different solution. The diffusion curves were measured by chronoamperometry (CA) method under a bias voltage of -150 mV over 120s. The full cell was assembled with Zn anode and cathodes separated by a glass fiber separator containing 100 ul MeOH-TI electrolyte for zinc-iodine battery. The I content of common battery test is 1.2 mg in each cell. The I content for low N/P ratio test is 4.2 mg and 6.6 mg in one cell. Glass fiber separator is 9 mg. Due to the low solubility of TI in water, TI was directly dip casted on cathode with same amount when testing performance in HOH with same I amount as in MeOH-TI. The thickness of zinc foil is 250 um. For low N/P ratio, the zinc foil is 25 um and 10 um. For the standard test and comparison, the gravimetric capacity is calculated based on the mass of active material I^- in organic iodide. All the cells were assembled to CR2032 coin cell in the air atmosphere with 750 psi. Low-temperature test was carried out by putting the assembled coin-cell type inside the mini freezer. Galvanostatic discharge-charge process was conducted on a Neware Battery Testing System ((CT-4008T-5V20mA-164, CT-4008T-5V50mA-164, CT-4008T-5V6A-S1, Shenzhen, China) and EIS in a frequency range of 10^{-1}-10^{6} Hz were performed on Bio Logic electrochemical workstation.

1.5 Computational methods

Geometry optimizations and frequency calculations of five binding structures (TI, $[TI_2]^+$, TI_3, $[Zn(MeOH)_6]^{2+}$, $[ZnI(MeOH)_5]^+$) and their components ($[T]^+$, I^-, I_2, I_3^-, Zn^{2+}, MeOH) were performed by Gaussian 16 combined with M06-2X/def2-SVP level and SMD (MeOH) implicit solvation model was used. Then the adsorption energy (E_{ad}) between three iodides and $[T]^+$, free energy change in the Zn^{2+} solvation and halogenated transformation processes were obtained.

Molecular dynamics (MD) simulations of blank and experimental electrolyte systems were performed using GROMACS 2021.5 package. Iodine and zinc used the van der Waals parameters inherent in Amberff14sb force filed. Ambertools21[3] and ACPYPE were used to construct the general AMBER force field 2(GAFF2) parameters of OTf^-, $[T]^+$ and MeOH, Multiwfn was used to fit the restrained electrostatic potential 2 (RESP2) charge of OTf^-, $[T]^+$, MeOH and I_3^- based on DFT calculation. The bonded parameters of I_2 and I_3^- were generated using Sobtop.

Blank electrolyte system was packed with 140 $Zn(OTf)_2$ (1 M) and 3150 MeOH, and experimental system was packed with 140 $Zn(OTf)_2$ (1 M), 14 $[T]^+$, 12 I^-, 6 I_2, 2 I_3^- (0.1 M, I^-:I_2:I_3^- = 6:3:1) and 3020 MeOH by packmol program, then energy minimization was performed by using the steepest descent algorithm with a force tolerance of 500 kJ mol^{-1} nm^{-1}. In all the three directions, periodic boundary conditions were imposed. Then these systems were relaxed for 1 ns under NPT ensemble and box size eventually stabilized at 6.2×6.2×6.2 nm^3.

After completing the above steps, 20 ns NPT MD simulations were performed. Pressure was maintained at 1 bar by the Parrinello-Rahman barostat in an isotropic manner and temperature was maintained at 298 K by the V-rescal thermostat. Lennard-Jones interactions were calculated within a cutoff of 1.2 nm, and electrostatic interactions beyond 1.2 nm were treated with particle-mesh Ewald (PME) method with a grid spacing of 0.16 nm. UCSF ChimeraX was used to visualize results.

2. Supplemental Figures

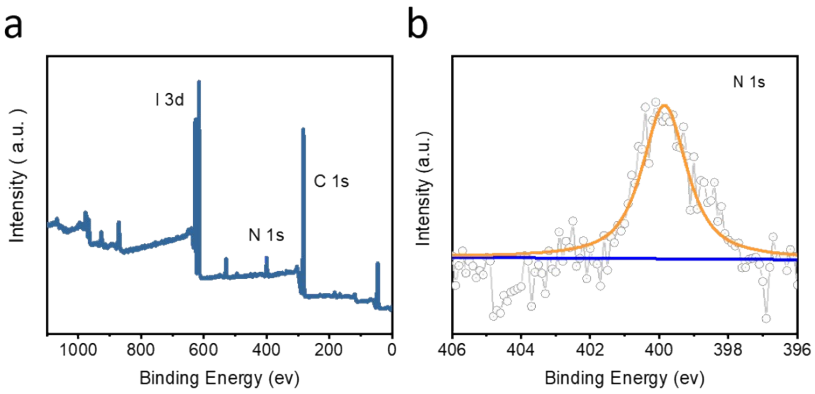

Figure. S1. a) All-element XPS spectra of TI. b) Detailed N 1s XPS profile. Three elements of C, N, and I are detected in the survey XPS spectrum as expected.

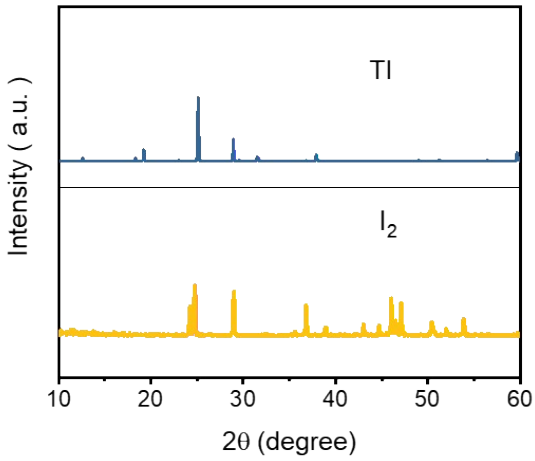

Figure. S2. XRD profile of TI and I_2.

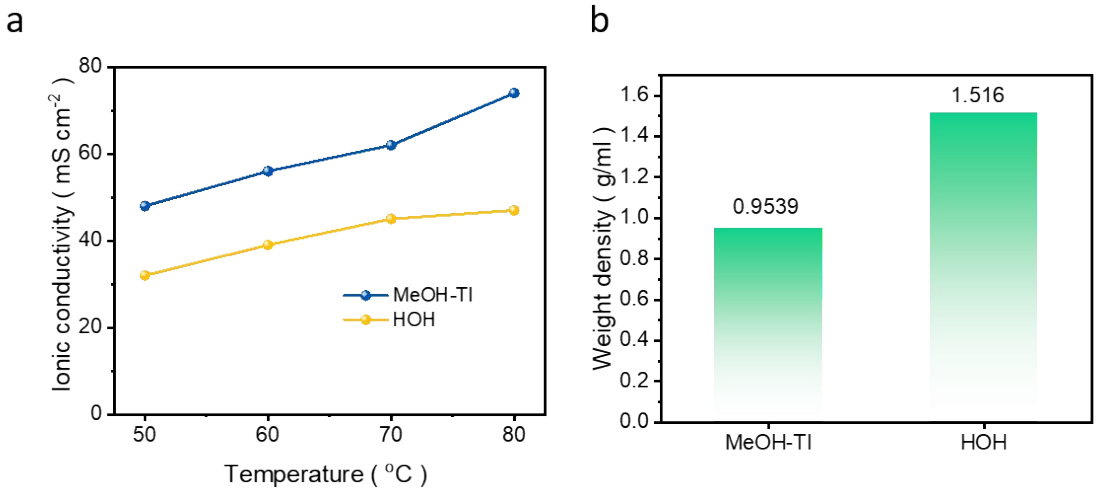

Figure. S3. a) Ionic conductivity of MeOH-TI and HOH at different temperatures. b) Weight density of MeOH-TI and HOH.

Note: The measured ionic conductivity value for MeOH-TI are all higher than HOH at different temperatures, demonstrating the rapid ion migration. It is worth noting that as the temperature increases, the charge transfer resistance decreases, and the slope of the line also rises, indicating an increase in the diffusion coefficient. Meanwhile, the electrolyte weight: MeOH-TI is 0.9539 g/ml and HOH is 1.516 g/ml. This phenomenon is mainly due to the much lower density of methanol with 0.792 g/ml compared to water with 0.998 g/ml. Since the weight of designed MeOH-TI is light, this may contribute to the increased total energy density when considering the reduced electrolyte weight content in the battery assembly packaging.

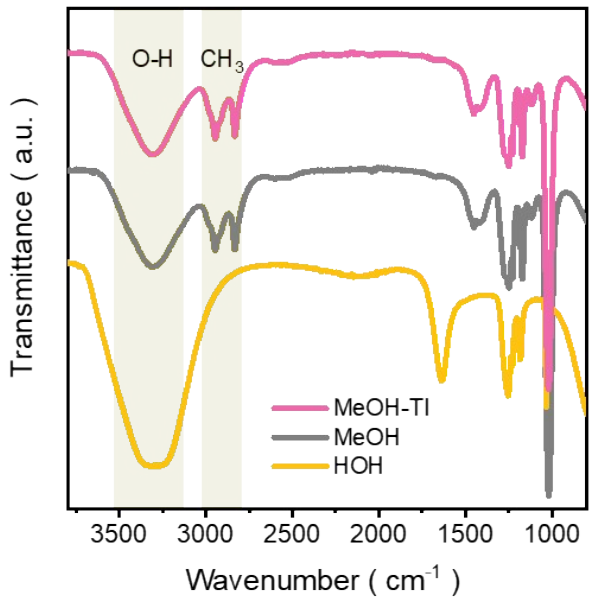

Figure. S4. FTIR spectra of MeOH-TI, MeOH and HOH.

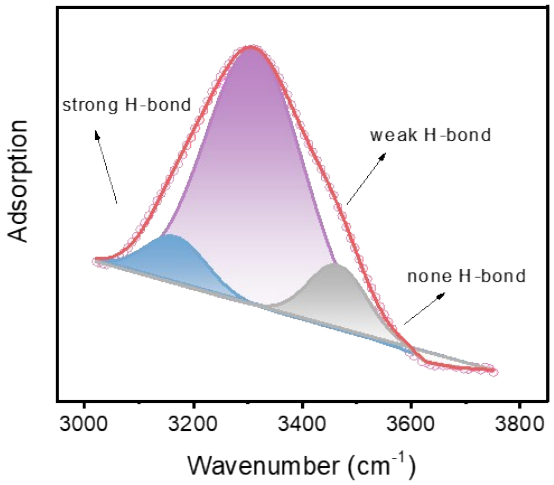

Figure. S5. The fitted FTIR spectra of the fitted H-bond for HOH.

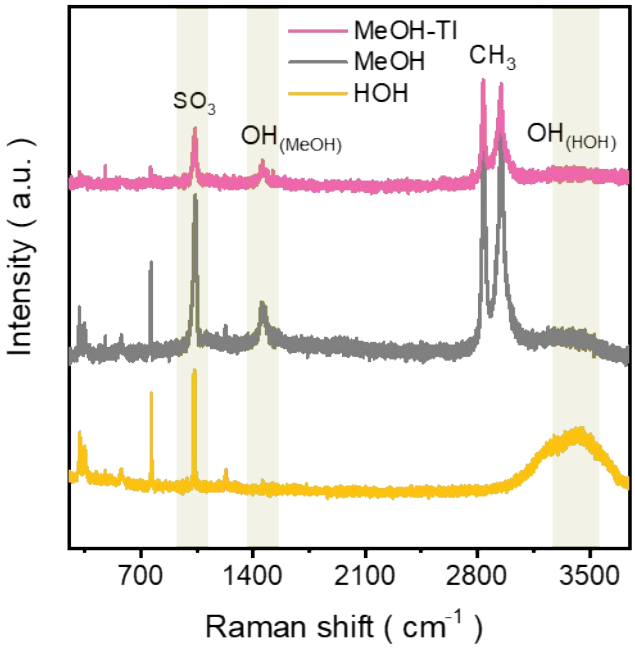

Figure. S6. Raman spectra for MeOH-TI, MeOH and HOH.

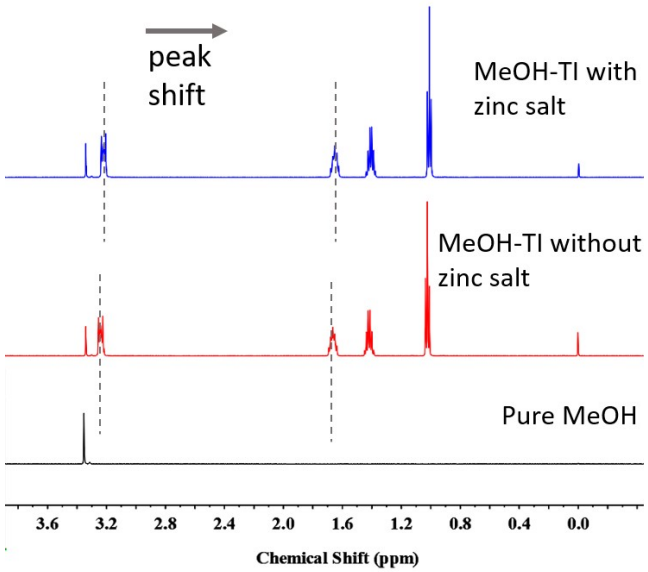

Figure. S7. ^{1}H NMR of pure MeOH, MeOH-TI with/without zinc salt.

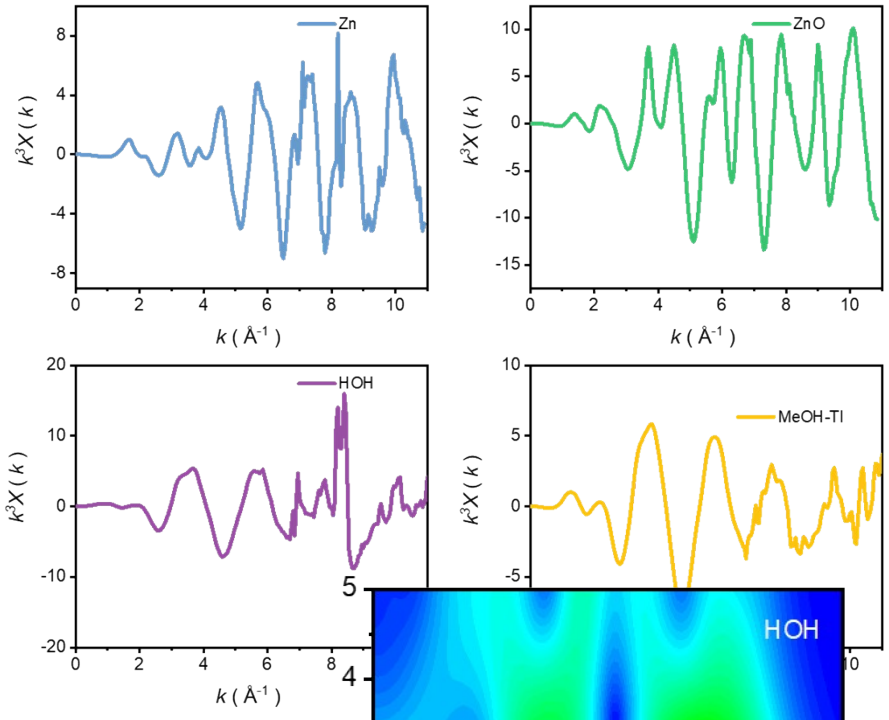

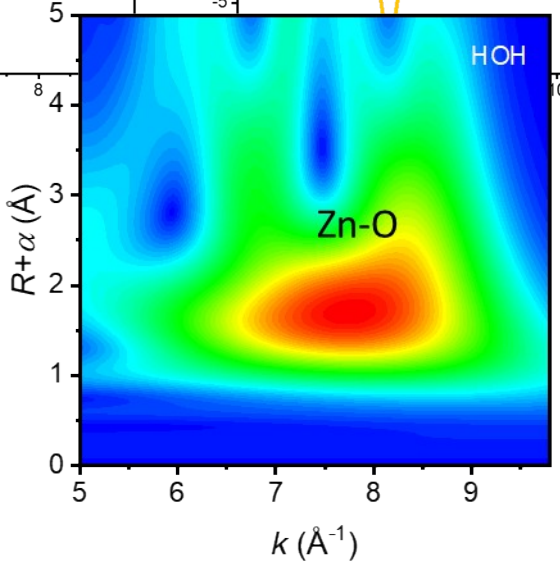

Figure. S8. *k*3-weighted Fourier transform of Zn *K*-edge EXAFS spectra in the *k*-space.

Figure. S9. Wavelet transforms of Zn K-edge XANES signals for HOH.

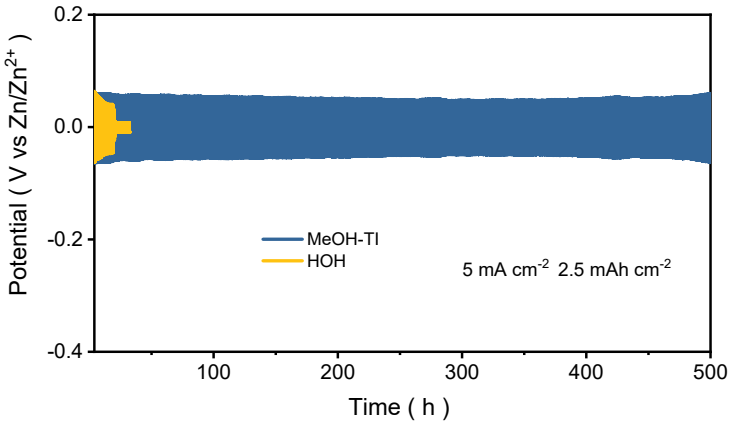

Figure. S10. Long-term galvanostatic cycling at 5 mA cm^{-2} and 2.5 mAh cm^{-2}.

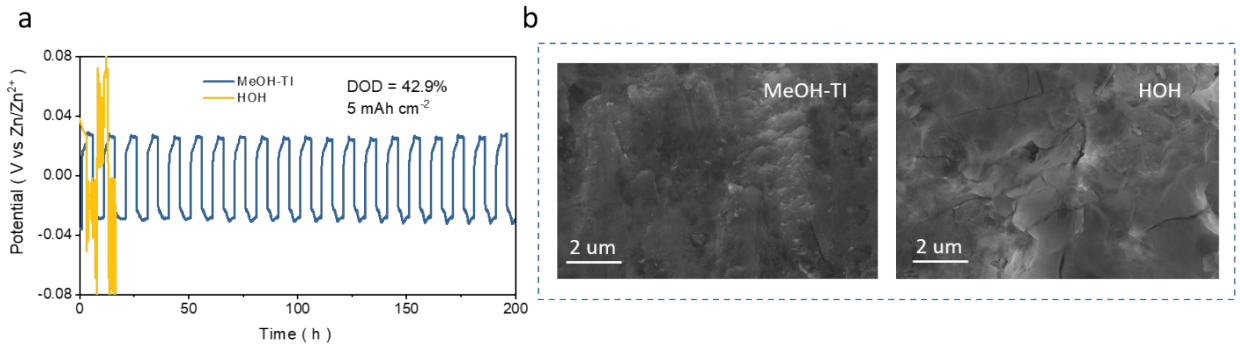

Figure. S11. a) Cycling performance in symmetric cell under high DOD condition, b) SEM images of zinc surface after cycling under high DOD condition in MeOH-TI and HOH.

Note: At high deposition capacity of 5 mAh cm^{-2}, loose structures are observed on Zn electrode using HOH, which is due to the rampant deposition induced by the local electric field intensity. On the contrary, the corresponding SEM images of the Zn electrode in the cell using MeOH-TI presents a greatly improved Zn deposition behavior, resulting in a compact Zn metal layer.

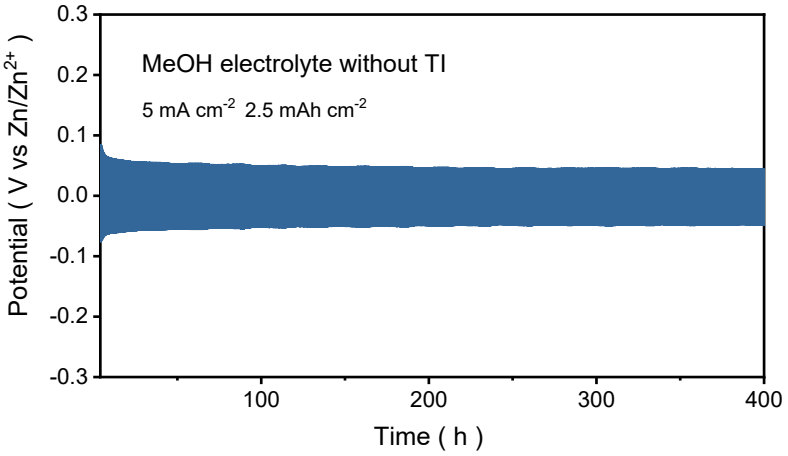

Figure. S12. Cycling performance of symmetrical cell in MeOH electrolyte without TI.

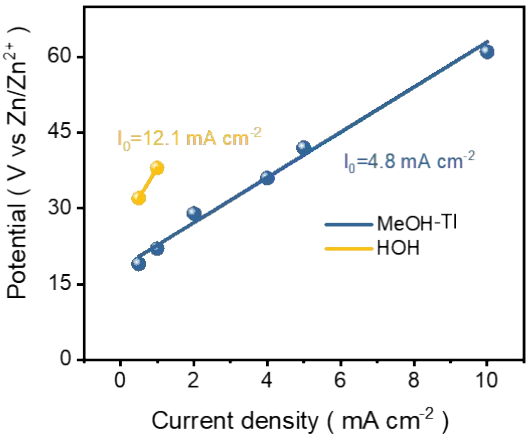

Figure. S13. Curves of potential against the current density of MeOH-TI, HOH.

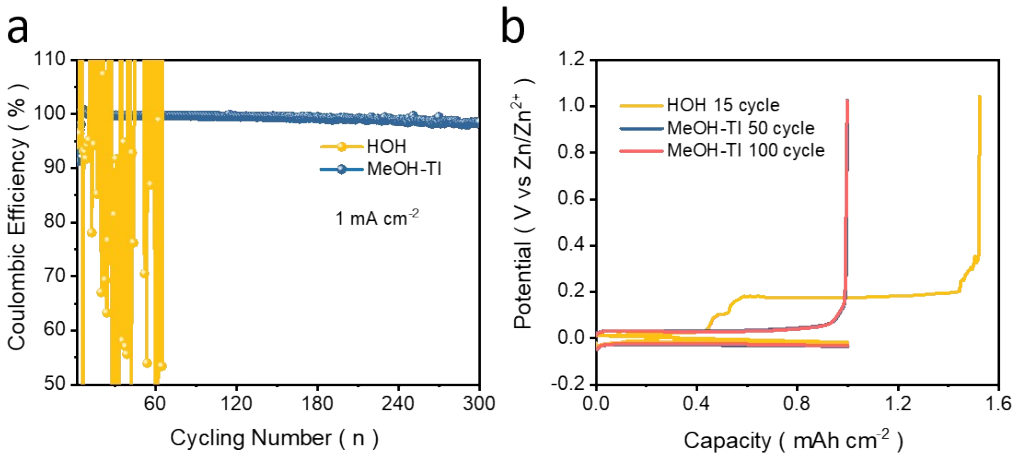

Figure. S14. a) CE of Zn plating and stripping at 1 mA cm^{-2}. b) Voltage profiles of Zn-Cu half-cell at 1 mA cm^{-2}.

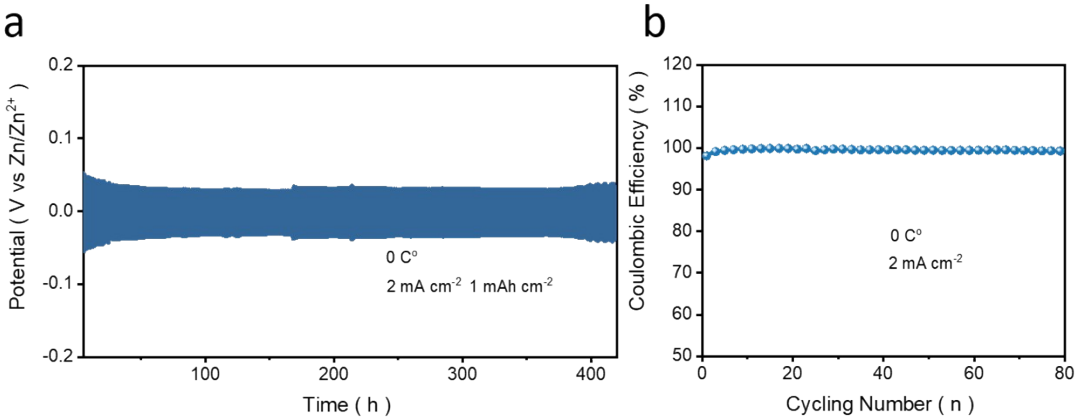

Figure. S15. a) Voltage-time profiles of the symmetrical cell at 0 °C. b) CE of Zn plating and stripping at at 0 °C.

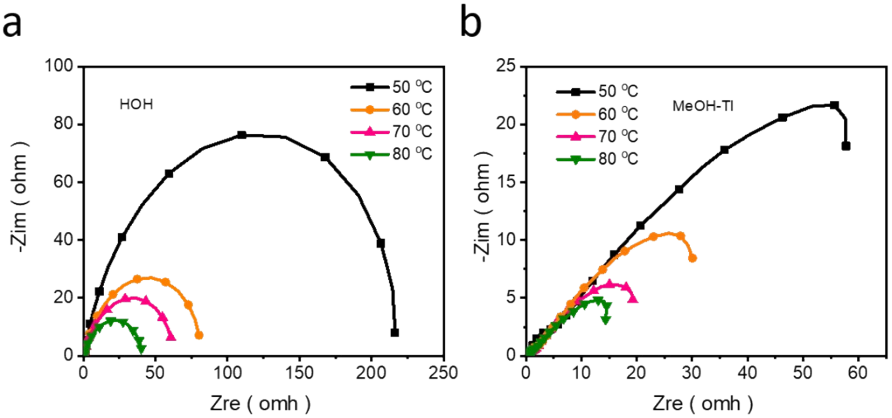

Figure. S16. Nyquist patterns at different temperatures of a) HOH, b) MeOH-TI.

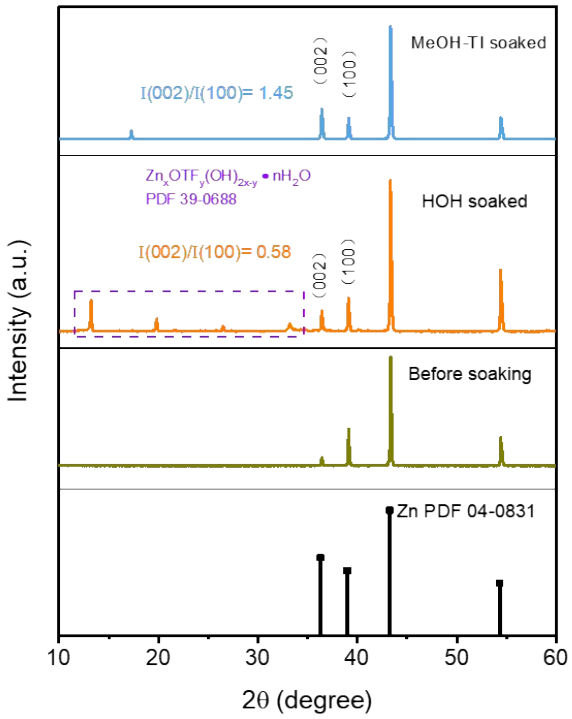

Figure. S17. XRD patterns of Zn foils before and after soaking.

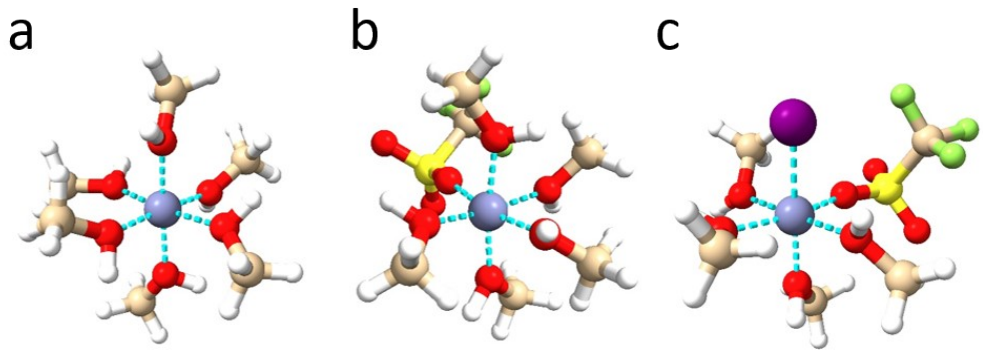

Figure. S18. a), b) The corresponding solvation structures in MeOH. c) The participation of I^- in solvation shell.

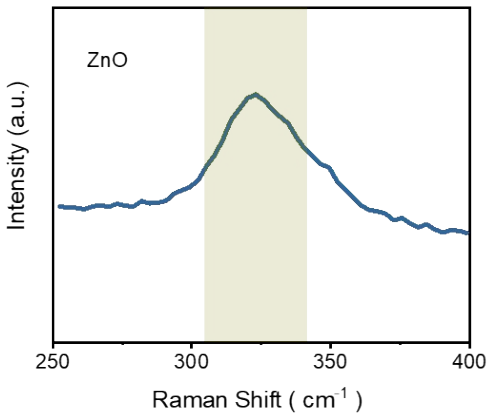

Figure. S19. Raman spectra of Zn electrode after cycling in MeOH-TI.

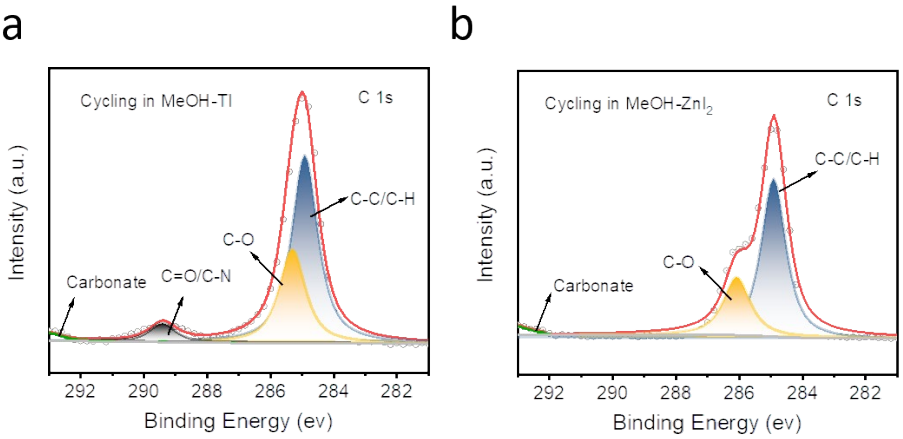

Figure. S20. XPS profiles of C *1s* for zinc electrode after cycling in MeOH-TI and MeOH-ZnI_2.

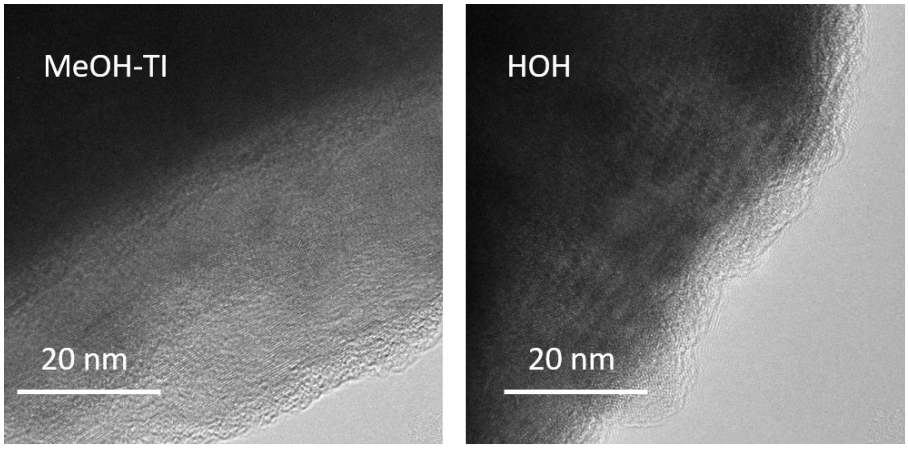

Figure. S21. TEM images of zinc surface morphologies before and after initial cycles in MeOH-TI.

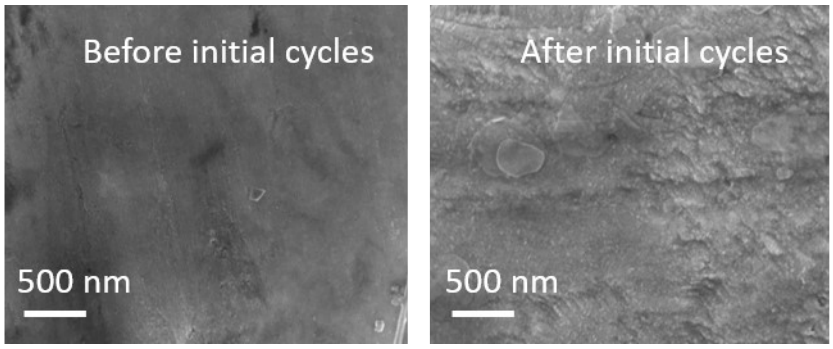

Figure. S22. SEM images of zinc surface morphologies before and after initial cycles in MeOH-TI.

Note: The bare electrode was uniformly covered with corrugate-shaped area for zinc deposition after 10 initial cycles, affirming the possible presence of SEI.

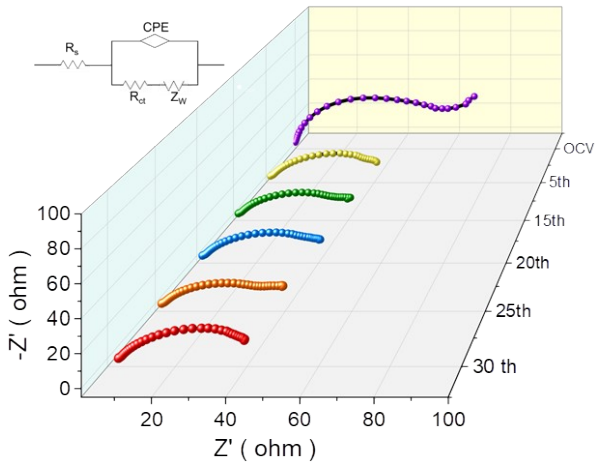

Figure. S23. EIS curves of batteries at different cycles in MeOH-TI in Zn//Zn symmetric cells.

Note: The EIS curves exhibits a characteristic pattern featuring a semicircle in the high-frequency region and a slanted line in the low-frequency region. Randle's equivalent circuit is employed to analyze the Nyquist plots, where *R*s denotes the ohmic resistance, *R*ct the charge transfer resistance, CPE the constant phase element, and *Z*w the Warburg resistance. The charge transfer resistances gradually decrease and remain basically constant after 15 cycles, implying formation of stable, hybrid SEI layer can occur in the early electrochemical process. Notably, the cell with MeOH-TI at open circuit voltage demonstrates a pronounced Warburg behavior, indicating faster bulk electrolyte diffusion. After the first 5 cycles activation, the charge transfer resistances experience greatly drop. Then, the charge transfer process remains basically stable at the interface and primarily involves for the subsequent cycles desolvation, adsorption, benefitting the stable SEI formation and uniform deposition.

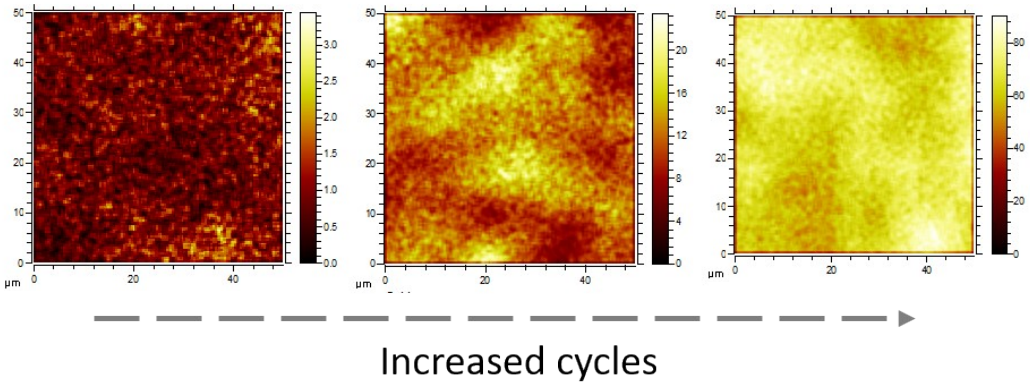

Figure. S24. TOF-SIMS ion mapping of F^- at initial increasing cycles.

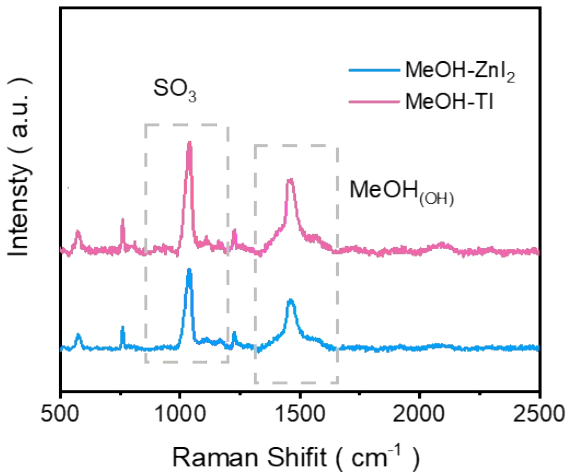

Figure S25. Raman spectra of MeOH-TI and MeOH-ZnI_2.

Note: It is observed that there is no obvious change of the electrolyte structure for both electrolytes. Combined with XPS results of SEI, we believe that solvation structure will not be influenced greatly upon changing TI with ZnI_2. While for the SEI formation, the T^+ cation also contribute to inorganic/organic layer to prevent the iodide-involved side reactions. This difference may attribute to irreversible charging/discharging in cell with MeOh-ZnI_2.

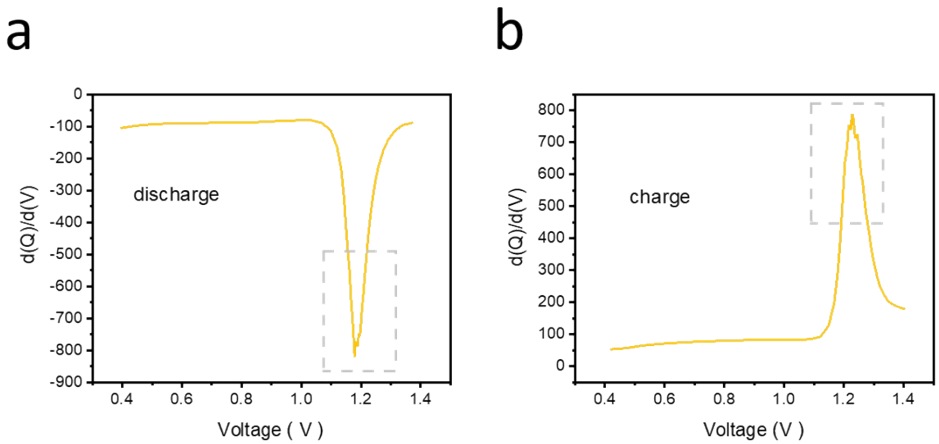

Figure S26. Differential capacity analysis of MeOH-TI during discharge and charge. The discharge and charge voltage plateaus for MeOH-TI are 1.18 V, 1.23 V, respectively.

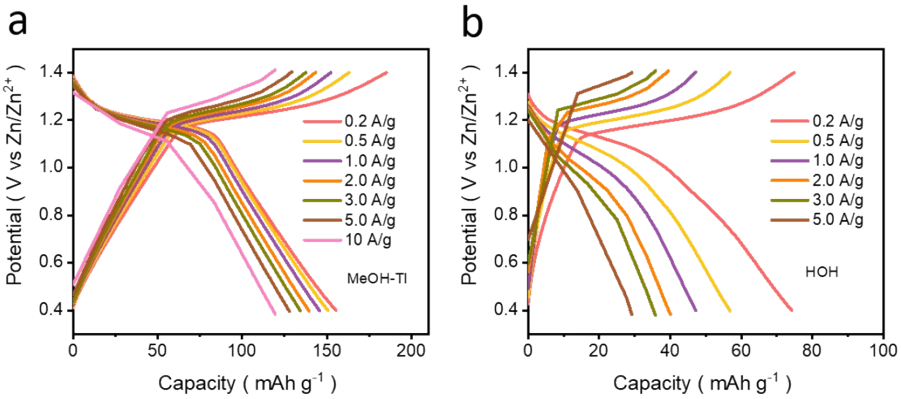

Figure. S27. GDC curve of a) MeeOH-TI, b) HOH in rate performance.

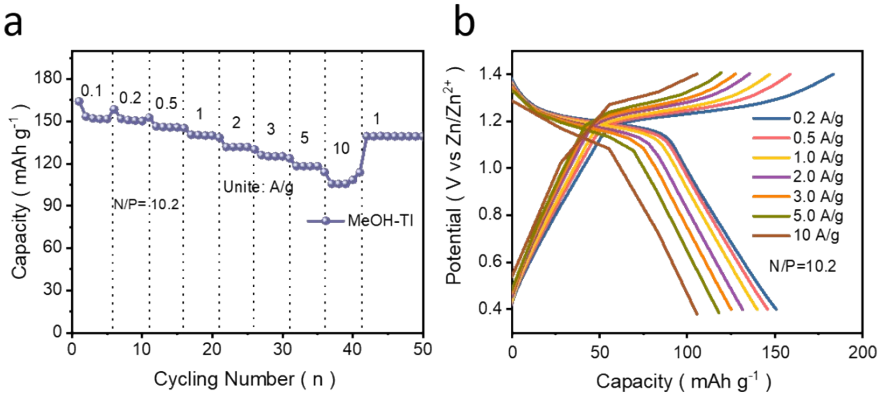

Figure. S28. a) Rate performances of zinc-iodine batteries in MeOH-TI with N/P ratio of 10.2. b) GCD curves of zinc-iodine batteries in MeOH-TI with low N/P ratio.

Note: The specific capacity still can maintain 118 mAh g^{-1} at 5 A g^{-1} with low N/P, indicating its superior rate capability

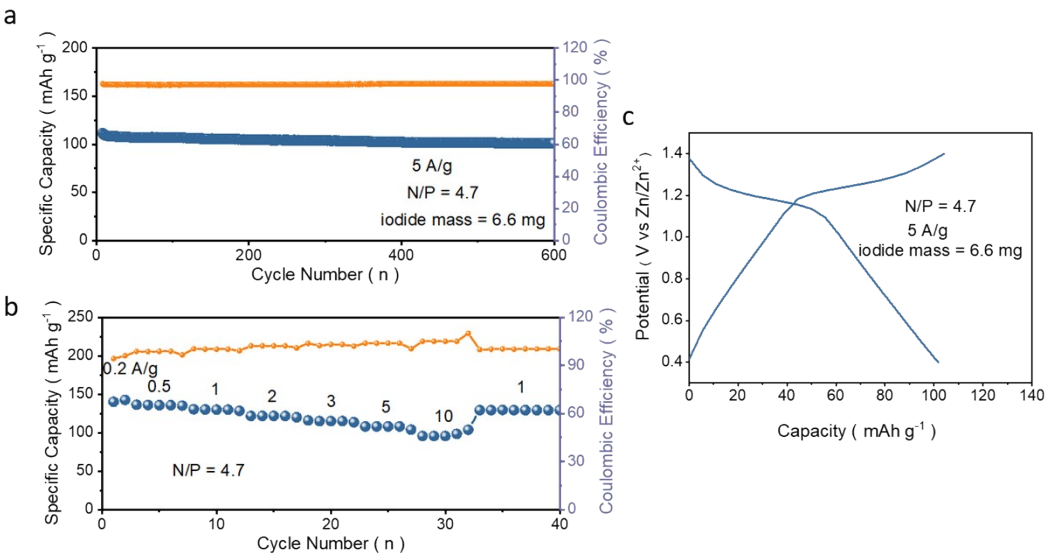

Figure. S29. a) Cycling performance with N/P ratio of 4.7, b) Rate performance with N/P ratio of 4.7, c) Charge/discharge curve of N/P ratio of 4.7.

Note: The mass of iodide active material achieved in the laboratory is 6.6 mg for each cell with lean electrolyte of 100 ul and the smallest zinc foil thickness is 10 um with weight of 7.9 mg.

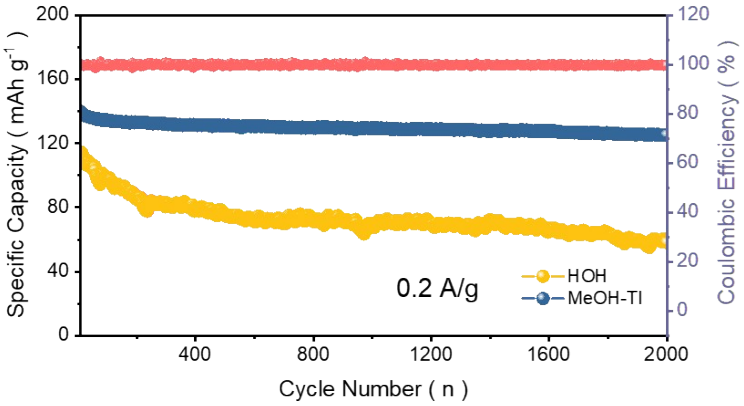

Figure. S30. Cycling performance of MeOH-TI, HOH at 0.2 A/g.

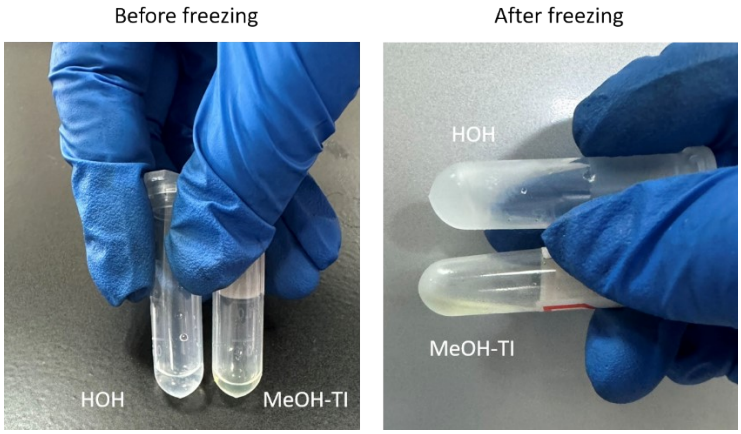

Figure. S31. Digital images of MeOH-TI and HOH before and after freezing at -20 ºC.

Note: The solidification was detected in HOH after freezing at -20 ºC, while the liquid state can still be maintained in MeOH-TI without any phase separation.

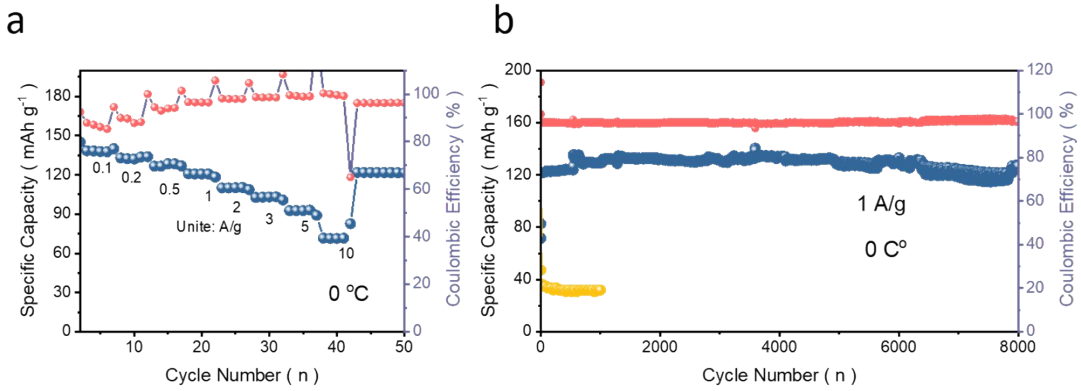

Figure. S32. a) Rate performance at 0 ºC. b) Cycling performance at 0 ºC.

Note: Due to the inevitable cross-over effect of iodides species and participation of iodides into superhalide solvation structure, the batteries with iodides within electrolyte will be influenced and result in relatively decreased CE.

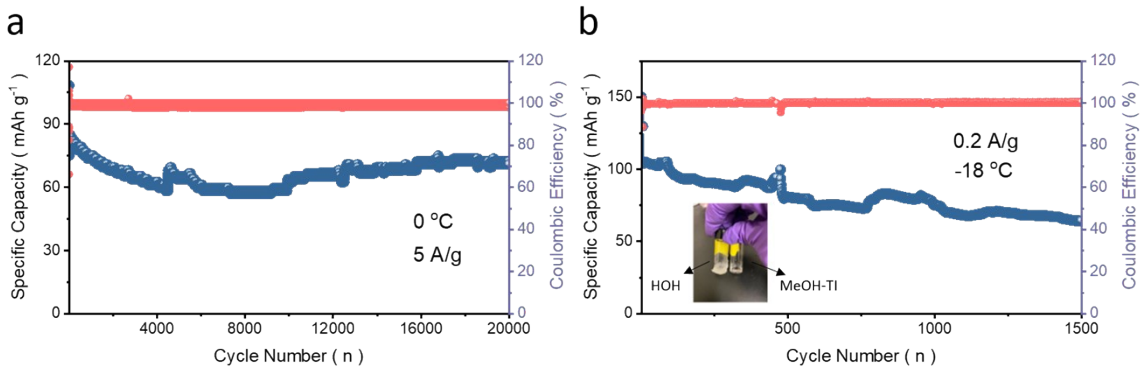

Figure. S33. a) Cycling performance at 0 °C at 5A/g. b) Cycling performance at -18 °C at 0.2 A/g.

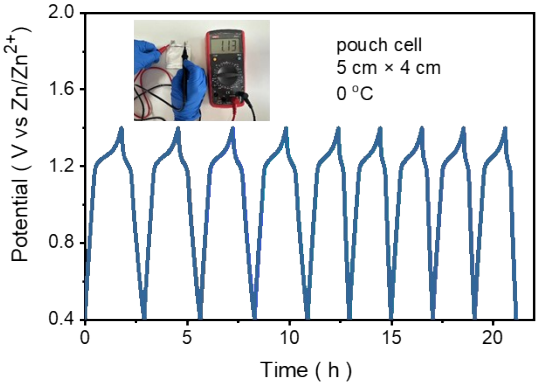

Figure. S34. Cycling performance in pouch cell at 0 °C.

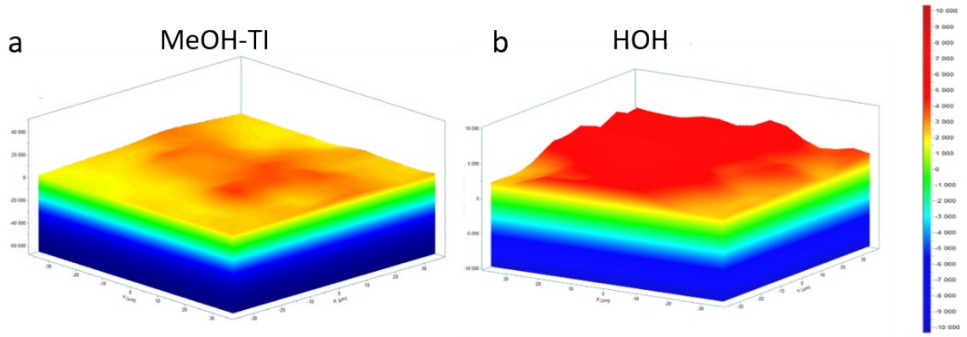

Figure. S35. a) 3D Raman spectra of zinc surface after cycling in low-temperature condition with MeOH-TI, b) 3D Raman spectra with HOH.

Note: MeOH-TI enables dense deposition and maintain smooth surface after low temperature operation, confirming the anti-freezing function of rearranged coordination solvation structure. In contrast, the morphology of bare electrode evolves into discontinuous islands after plating in HOH, indicating the modulations of hydrogen bonding and cation-anion interactions are not strong enough to suppress initial ice nucleation.

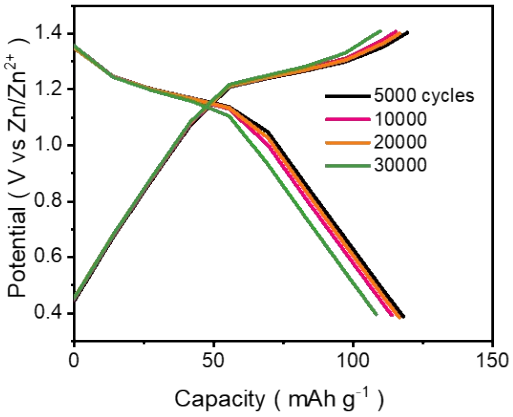

Figure. S36. Galvanostatic discharge-charge profiles at different cycles at 5 A/g.

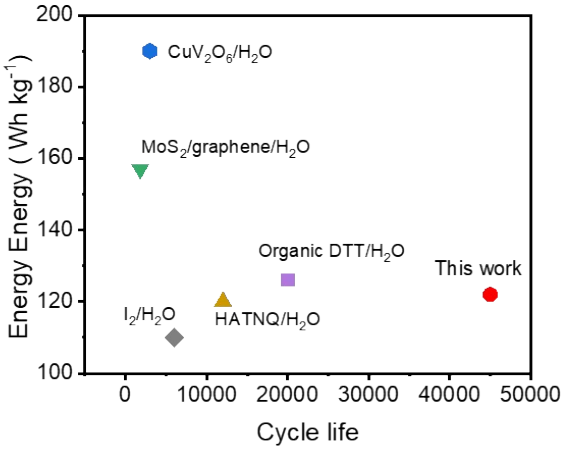

Figure. S37. Literature survey of rechargeable Zn batteries with representative cathode materials and their corresponding electrolyte systems.

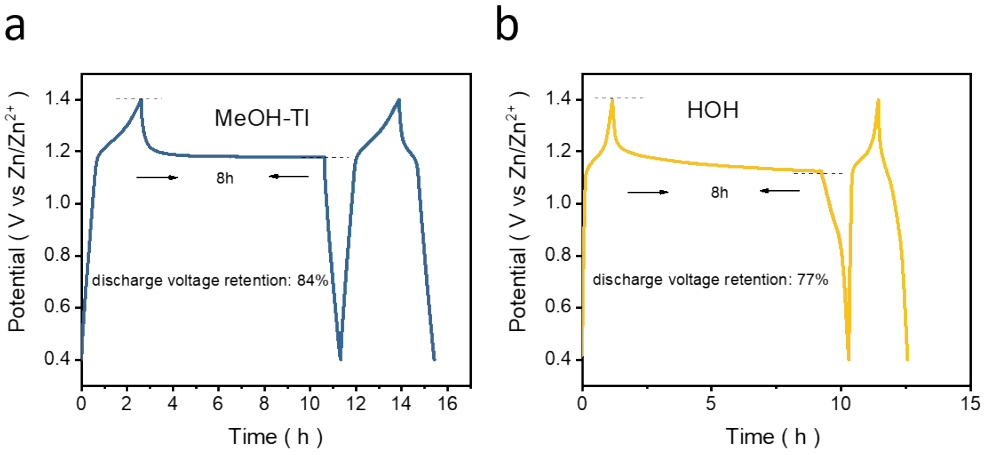

Figure. S38. Resting curves of a) MeOH-TI, b) HOH.

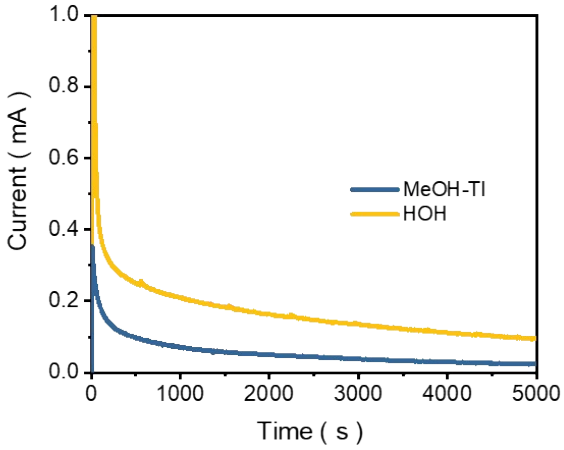

Figure. S39. Float charge current test of MeOH-TI and HOH.

Note: Lower floating charge current in MeOH-TI indicates smaller amount of energy required to maintain the stability of electrolyte and battery.

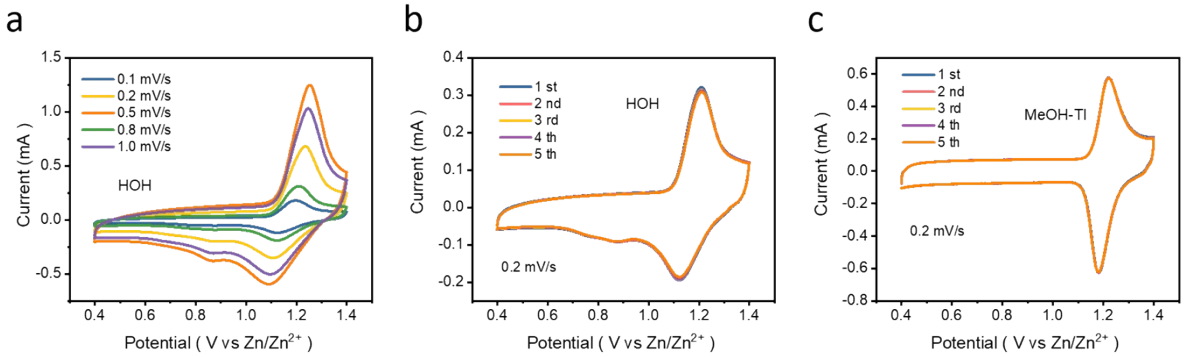

Figure. S40. a) CV curves of HOH at various scan rates. b) CV curves of HOH at 0.2 mV/s. c) CV curves of MeOH-TI at 0.2 mV/s.

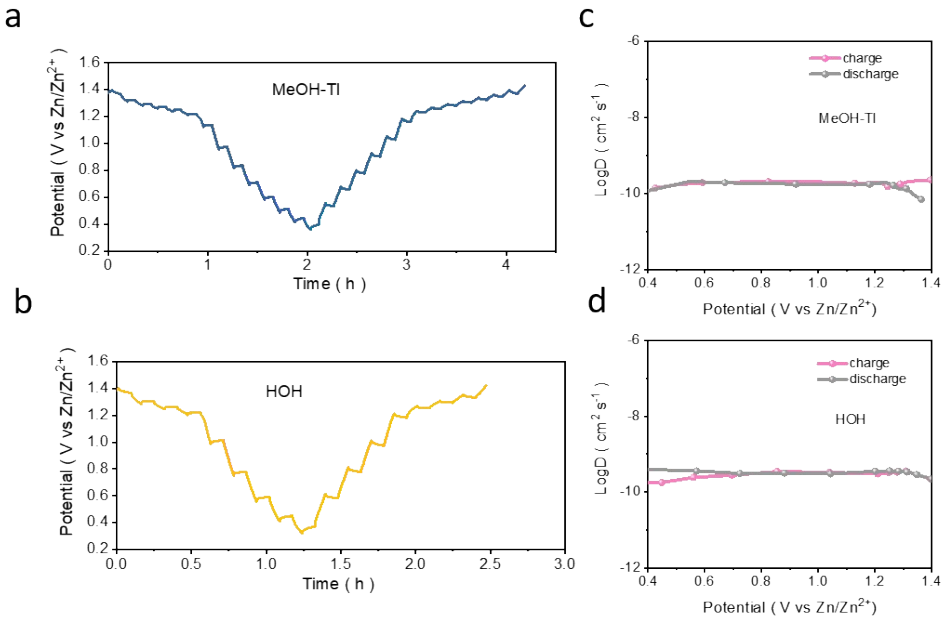

Figure. S41. GITT curves of a) MeOH-TI and b) HOH, Diffusion coefficient of c) MeOH-TI and d) HOH.

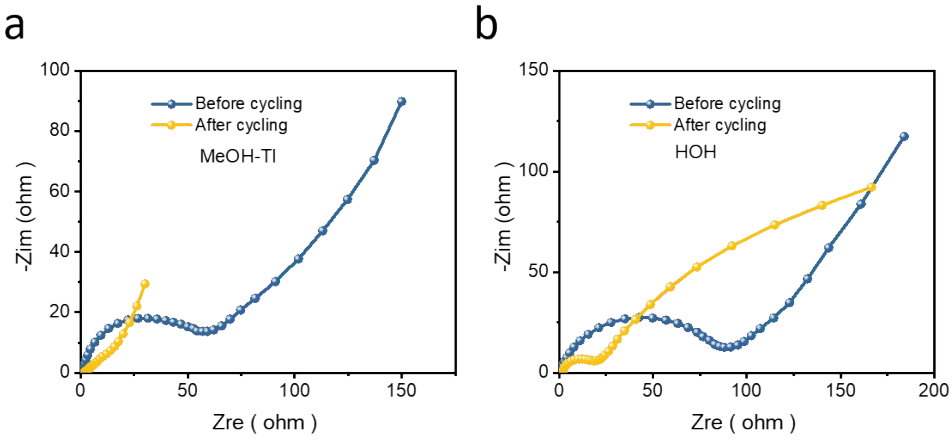

Figure. S42. Nyquist plots from EIS test in full cell before cycling at open circuit voltage and after cycling at charging voltage.

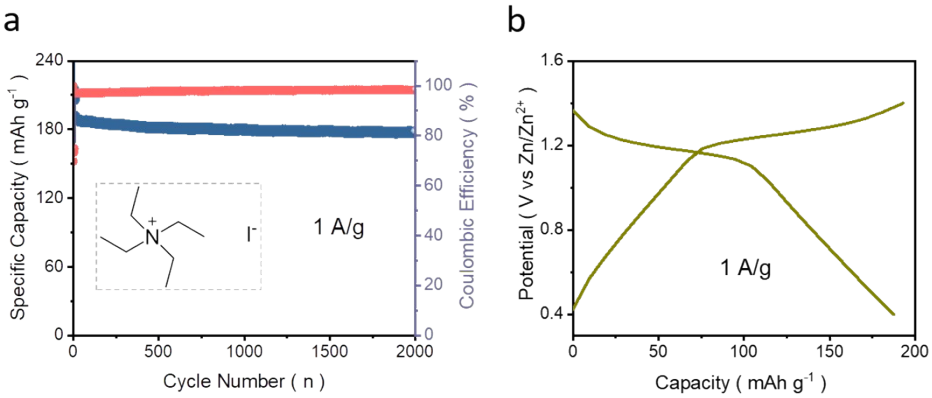

Figure. S43. a) Cycling performance of zinc-iodine batteries using tetraethylammonium iodide with shorter organic group as iodine salt. b) Charge/discharge voltage profile of battery using tetraethylammonium iodide.

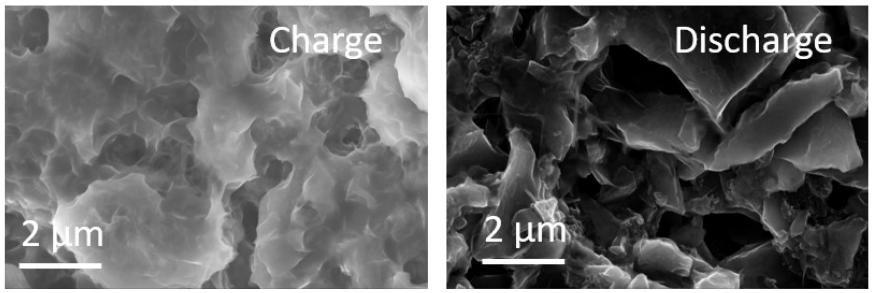

Figure. S44. SEM images of cathode after charge and discharge.

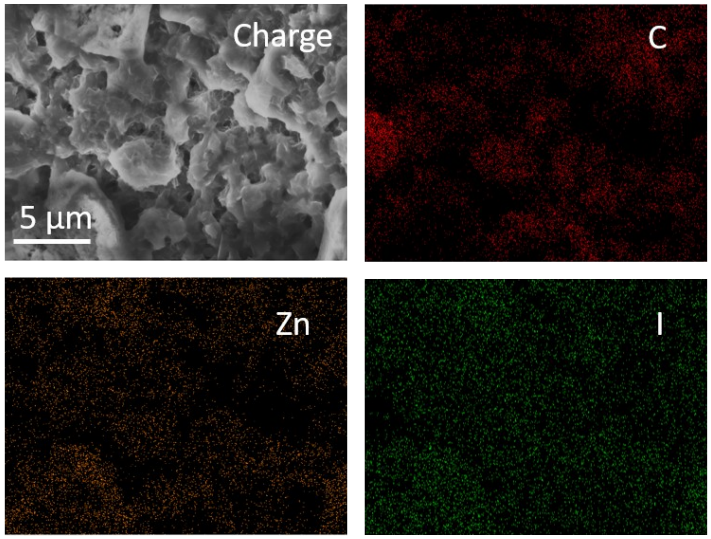

Figure. S45. SEM and EDX mapping images of cathode after charging.

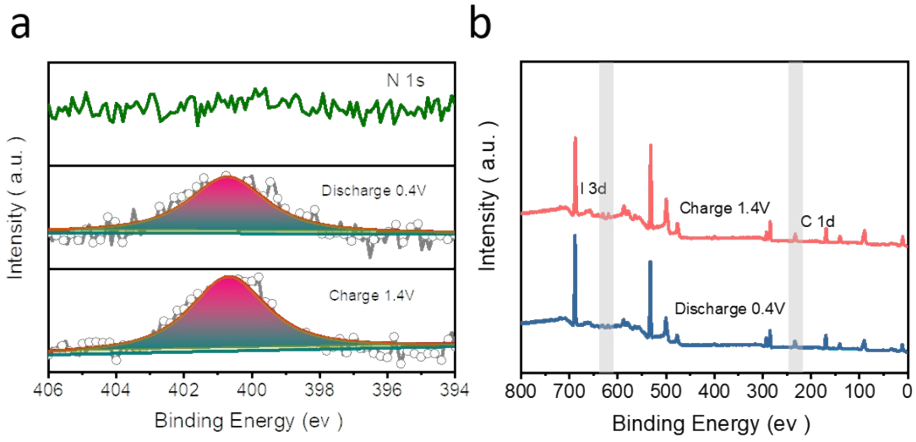

Figure. S46. a) XPS of N 1s after charge and discharge. b) All-element XPS spectra after charge and discharge.

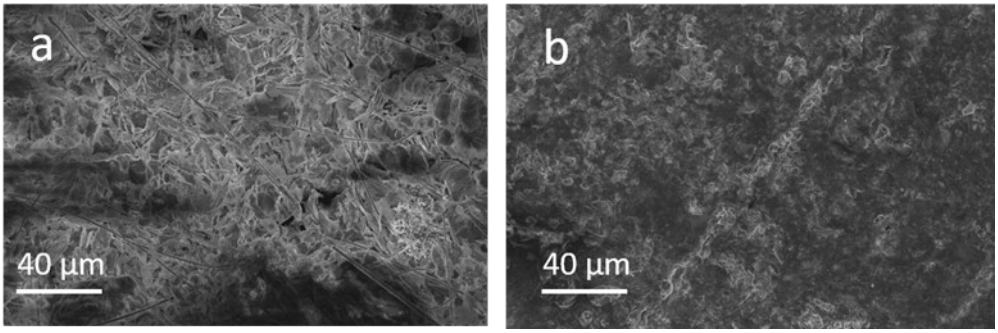

Figure. S47. SEM images of zinc surface after cycling in full cells in a) HOH, b) MeOH-TI.

3. Supplemental Tables

Table S1. Comparison of main parameters and cycling property for this work with recently reported strategies for zinc-iodine batteries.

Strategies	Current density ($A\ g^{-1}$)	Specific capacity ($mAh\ g^{-1}$)	Cycling life (h)	Energy density ($Wh\ kg^{-1}$)	Ref
$HCNS/I_{0.5}$	0.2	143	1500		1
PTC interlayer	10	115	20000		2
GC-PAN/I	10	130.5	2000	159.5	3
$Zn/C\text{-}I_2$	1	139	500		4
N-rGO	5	130	1500		5
$G/PVP@ZnI_2$	1	125	1000	162	6
IC5 gel	1	105	500		7
MeOH-TI	**10**	**119**	**20000**	**155**	**This work**
	5	**127**	**45000**		

Table S2. Comparison of the recently reported zinc-iodine batteries performance at low temperature.

Strategies	Current density ($A\ g^{-1}$)	Specific capacity ($mAh\ g^{-1}$)	Temperature (^oC)	Ref
PAM-based HE	50	39	-20	8
$Zn(ClO_4)_2$ -ACN	5	105	/	9
MeOH-TI	**1**	**109**	**0**	**This work**
	0.2	**105**	**-18**	

Table S3. Summary of representative strategies for high I loading and limited zinc supply in zinc-iodine batteries.

Strategies	Cycling stability (mA cm^{-2}) @ A g^{-1}	Capacity (mAh g^{-1})	Iodine loading (mg)	Zinc foil thickness (um)	Ref
LA133	1000@0.2	102	7.8	200-250	10
PNC-1000-I_2	6000@0.4	200	6	200-250	11
EI-ZrP/I_2	10000@1	140	4.6	200-250	12
I_2/OSTC	10000@1	157	4	200-250	13
PC@Fe_2N-x/I_2	500@2	135	4.5	200-250	14
Zn-CCS||I2/AC	15000@2	130	3	200-250	15
MeOH-TI	**45000@5**	**124**	**1.2**	**250**	**This work**
	600@5	**102**	**6.6**	**10**	

4. References

1. Chai, Lulu, et al. "In-MOF-Derived Hierarchically Hollow Carbon Nanostraws for Advanced Zinc-Iodine Batteries." Advanced Science 9.33 (2022): 2105063.
2. Zhang, Ying, et al. "Flexible PEDOT: PSS nanopapers as “anion-cation regulation” synergistic interlayers enabling ultra-stable aqueous zinc-iodine batteries." Journal of Energy Chemistry 75 (2022): 310-320.
3. Zhang, Leiqian, et al. "A Universal Polyiodide Regulation Using Quaternization Engineering toward High Value-Added and Ultra-Stable Zinc-Iodine Batteries." Advanced Science 9.13 (2022): 2105598.
4. Yan, Lijing, et al. "Multifunctional porous carbon strategy assisting high-performance aqueous zinc-iodine battery." Carbon 187 (2022): 145-152.
5. Dang, Hoang X., Andrew J. Sellathurai, and Dominik PJ Barz. "An ion exchange membrane-free, ultrastable zinc-iodine battery enabled by functionalized graphene electrodes." Energy Storage Materials 55 (2023): 680-690.
6. Zhang, Yixiang, et al. "Iodine Promoted Ultralow Zn Nucleation Overpotential and Zn-Rich Cathode for Low-Cost, Fast-Production and High-Energy Density Anode-Free Zn-Iodine Batteries." Nano-Micro Letters 14.1 (2022): 208.
7. Sonigara, Keval K., et al. "Self-Assembled Solid-State Gel Catholyte Combating Iodide Diffusion and Sel-Discharge for a Stable Flexible Aqueous Zn–I_2 Battery." Advanced Energy Materials 10.47 (2020): 2001997.
8. Chen, Chaojie, et al. "High-Energy Density Aqueous Zinc–Iodine Batteries with Ultra-long Cycle Life Enabled by the ZnI_2 Additive." ACS Sustainable Chemistry & Engineering 9.39 (2021): 13268-13276.
9. Song, Chunlai, et al. "High performance Zn-I2 battery with acetonitrile electrolyte working at low temperature." Nano Research (2022): 1-8.
10. Wang, Kexuan, et al. "An Iodine-Chemisorption Binder for High-Loading and Shuttle-Free Zn–Iodine Batteries." Advanced Energy Materials (2024): 2304110.
11. Liu, Tingting, et al. "Recognition of the catalytic activities of graphitic N for zinc-iodine batteries." Energy Storage Materials 53 (2022): 544-551.
12. Wu, Jiawen, et al. "Immobilizing Polyiodides with Expanded Zn^{2+} Channels for High-Rate Practical Zinc-Iodine Battery." Advanced Energy Materials 14.3 (2024): 2302738.

13. Chen, Mengyu, et al. "Tightly confined iodine in surface-oxidized carbon matrix toward dual-mechanism zinc-iodine batteries." Energy Storage Materials 59 (2023): 102760.
14. Chen, Qianwu, et al. "Synergic anchoring of Fe_2N nanoclusters on porous carbon to enhance reversible conversion of iodine for high-temperature zinc-iodine battery." Nano Energy 117 (2023): 108897.
15. Hu, Zuyang, et al. "Crowding Effect-Induced Zinc-Enriched/Water-Lean Polymer Interfacial Layer Toward Practical Zn-Iodine Batteries." ACS nano 17.22 (2023): 23207-23219.